Complete measurement of three-body photodisintegration of ³He for photon energies between 0.35 and 1.55 GeV

S. Niccolai,[2,11,*] G. Audit,[2] B. L. Berman,[11] J. M. Laget,[2] S. Strauch,[11] G. Adams,[28] A. Afanasev,[38] P. Ambrozewicz,[9] M. Anghinolfi,[15] J. R. M. Annand,[12] C. Armstrong,[33] B. Asavapibhop,[21] H. Avakian,[33] H. Bagdasaryan,[25] J. P. Ball,[1] S. Barrow,[10] M. Battaglieri,[15] K. Beard,[18] M. Bektasoglu,[25] M. Bellis,[4] N. Benmouna,[11] N. Bianchi,[14] A. S. Biselli,[4] S. Boiarinov,[33] B. E. Bonner,[29] S. Bouchigny,[16] R. Bradford,[4] D. Branford,[8] W. J. Briscoe,[11] W. K. Brooks,[33] V. D. Burkert,[33] C. Butuceanu,[37] J. R. Calarco,[22] D. S. Carman,[24] B. Carnahan,[5] S. Chen,[10] P. L. Cole,[13] A. Coleman,[37,†] D. Cords,[33,‡] P. Corvisiero,[15] D. Crabb,[36] H. Crannell,[5] J. P. Cummings,[28] E. De Sanctis,[14] R. DeVita,[15] P. V. Degtyarenko,[33] H. Denizli,[27] L. Dennis,[10] K. V. Dharmawardane,[25] K. S. Dhuga,[11] C. Djalali,[31] G. E. Dodge,[25] D. Doughty,[6] P. Dragovitsch,[10] M. Dugger,[1] S. Dytman,[27] O. P. Dzyubak,[31] H. Egiyan,[33] K. S. Egiyan,[38] L. Elouadrhiri,[33] A. Empl,[28] R. Ent,[33] P. Eugenio,[10] R. Fatemi,[36] G. Fedotov,[39] G. Feldman,[11] R. J. Feuerbach,[33] J. Ficenec,[35] T. A. Forest,[25] H. Funsten,[37] G. Gavalian,[25] G. P. Gilfoyle,[30] K. L. Giovanetti,[18] E. Golovatch,[39,15] C. I. O. Gordon,[12] R. W. Gothe,[31] K. Griffioen,[37] M. Guidal,[16] M. Guillo,[31] N. Guler,[25] L. Guo,[33] V. Gyurjyan,[33] C. Hadjidakis,[16] R. S. Hakobyan,[5] J. Hardie,[6,33] D. Heddle,[33] P. Heimberg,[11] F. W. Hersman,[22] K. Hicks,[24] K. Hleiqawi,[24] M. Holtrop,[22] J. Hu,[28] M. Huertas,[31] C. E. Hyde-Wright,[25] Y. Y. Ilieva,[11] D. Ireland,[12] M. M. Ito,[33] D. Jenkins,[35] H. S. Jo,[16] K. Joo,[7] H. G. Juengst,[11] J. Kellie,[12] M. Khandaker,[23] K. Y. Kim,[27] K. Kim,[19] W. Kim,[19] A. Klein,[25] F. J. Klein,[5] A. V. Klimenko,[25] M. Klusman,[28] M. Kossov,[17] L. H. Kramer,[9,33] Y. Kuang,[37] S. E. Kuhn,[25] J. Kuhn,[4] J. Lachniet,[4] J. Langheinrich,[31] D. Lawrence,[21] Ji Li,[28] A. C. S. Lima,[11] K. Livingston,[12] K. Lukashin,[5] J. J. Manak,[33] C. Marchand,[2] S. McAleer,[10] J. W. C. McNabb,[26] B. A. Mecking,[33] J. J. Melone,[12] M. D. Mestayer,[33] C. A. Meyer,[4] K. Mikhailov,[17] R. Minehart,[36] M. Mirazita,[14] R. Miskimen,[21] L. Morand,[2] S. A. Morrow,[2] V. Muccifora,[14] J. Mueller,[27] L. Y. Murphy,[11] G. S. Mutchler,[29] J. Napolitano,[28] R. Naseripour,[9] G. Niculescu,[18] I. Niculescu,[18] B. B. Niczyporuk,[33] R. A. Niyazov,[33] M. Nozar,[33] J. T. O'Brien,[5] G. V. O'Rielly,[11] M. Osipenko,[39,15] A. Ostrovidov,[10] K. Park,[19] E. Pasyuk,[1] S. A. Philips,[11] N. Pivnyuk,[17] D. Pocanic,[36] O. Pogorelko,[17] E. Polli,[14] I. Popa,[11] S. Pozdniakov,[17] B. M. Preedom,[31] J. W. Price,[3] Y. Prok,[36] D. Protopopescu,[12] L. M. Qin,[25] B. A. Raue,[9,33] G. Riccardi,[10] G. Ricco,[15] M. Ripani,[15] B. G. Ritchie,[1] F. Ronchetti,[14] G. Rosner,[12] P. Rossi,[14] D. Rowntree,[20] P. D. Rubin,[30] F. Sabatié,[2] C. Salgado,[23] J. P. Santoro,[35,33] V. Sapunenko,[15] R. A. Schumacher,[4] V. S. Serov,[17] A. Shafi,[11] Y. G. Sharabian,[33] J. Shaw,[21] A. V. Skabelin,[20] E. S. Smith,[33] L. C. Smith,[36] D. I. Sober,[5] A. Stavinsky,[17] S. Stepanyan,[25,38] P. Stoler,[28] I. I. Strakovsky,[11] R. Suleiman,[20] M. Taiuti,[15] S. Taylor,[29] D. J. Tedeschi,[31] U. Thoma,[33,§] R. Thompson,[27] R. Tkabladze,[24] L. Todor,[30] C. Tur,[31] M. Ungaro,[28] M. F. Vineyard,[34] A. V. Vlassov,[17] K. Wang,[36] L. B. Weinstein,[25] D. P. Weygand,[33] C. S. Whisnant,[18,31] M. Williams,[4] E. Wolin,[33] M. H. Wood,[31] A. Yegneswaran,[33] J. Yun,[25] and L. Zana[22]

(The CLAS Collaboration)

[1]*Arizona State University, Tempe, Arizona 85287-1504, USA*
[2]*CEA-Saclay, Service de Physique Nucléaire, F91191 Gif-sur-Yvette, France*
[3]*University of California at Los Angeles, Los Angeles, California 90095, USA*
[4]*Carnegie Mellon University, Pittsburgh, Pennsylvania 15213, USA*
[5]*Catholic University of America, Washington, D.C. 20064, USA*
[6]*Christopher Newport University, Newport News, Virginia 23606, USA*
[7]*University of Connecticut, Storrs, Connecticut 06269, USA*
[8]*Edinburgh University, Edinburgh EH9 3JZ, United Kingdom*
[9]*Florida International University, Miami, Florida 33199, USA*
[10]*Florida State University, Tallahassee, Florida 32306, USA*
[11]*The George Washington University, Washington, D.C. 20052, USA*
[12]*University of Glasgow, Glasgow G12 8QQ, United Kingdom, USA*
[13]*Idaho State University, Pocatello, Idaho 83209, USA*
[14]*INFN, Laboratori Nazionali di Frascati, Frascati, Italy*
[15]*INFN, Sezione di Genova, 16146 Genova, Italy*
[16]*Institut de Physique Nucléaire ORSAY, F91406 Orsay, France*
[17]*Institute of Theoretical and Experimental Physics, Moscow 117259, Russia*
[18]*James Madison University, Harrisonburg, Virginia 22807, USA*
[19]*Kyungpook National University, Daegu 702-701, South Korea*
[20]*Massachusetts Institute of Technology, Cambridge, Massachusetts 02139, USA*
[21]*University of Massachusetts, Amherst, Massachusetts 01003, USA*
[22]*University of New Hampshire, Durham, New Hampshire 03824, USA*
[23]*Norfolk State University, Norfolk, Virginia 23504, USA*
[24]*Ohio University, Athens, Ohio 45701, USA*
[25]*Old Dominion University, Norfolk, Virginia 23529, USA*
[26]*Penn State University, University Park, Pennsylvania 16802, USA*
[27]*University of Pittsburgh, Pittsburgh, Pennsylvania 15260, USA*

^{28}*Rensselaer Polytechnic Institute, Troy, New York 12180-3590, USA*
^{29}*Rice University, Houston, Texas 77005-1892, USA*
^{30}*University of Richmond, Richmond, Virginia 23173, USA*
^{31}*University of South Carolina, Columbia, South Carolina 29208, USA*
^{32}*University of Texas at El Paso, El Paso, Texas 79968, USA*
^{33}*Thomas Jefferson National Accelerator Facility, Newport News, Virginia 23606, USA*
^{34}*Union College, Schenectady, New York 12308, USA*
^{35}*Virginia Polytechnic Institute and State University, Blacksburg, Virginia 24061, USA*
^{36}*University of Virginia, Charlottesville, Virginia 22901, USA*
^{37}*College of William and Mary, Williamsburg, Virginia 23187, USA*
^{38}*Yerevan Physics Institute, 375036 Yerevan, Armenia*
^{39}*Moscow State University, General Nuclear Physics Institute, 119899 Moscow, Russia*
(Received 17 September 2004; published 20 December 2004)

The three-body photodisintegration of ^{3}He has been measured with the CLAS detector at Jefferson Lab, using tagged photons of energies between 0.35 GeV and 1.55 GeV. The large acceptance of the spectrometer allowed us for the first time to cover a wide momentum and angular range for the two outgoing protons. Three kinematic regions dominated by either two- or three-body contributions have been distinguished and analyzed. The measured cross sections have been compared with results of a theoretical model, which, in certain kinematic ranges, have been found to be in reasonable agreement with the data.

I. INTRODUCTION

The study of the electromagnetic properties of the ^{3}He nucleus is the optimal starting point to assess the importance of many-body interactions between nucleons in nuclei [1,2]. In particular, in the $\gamma\,^3\text{He}\rightarrow ppn$ reaction, three-nucleon currents dominate in certain regions of phase space [3–5]. In fact, a pp pair has no dipole moment with which to couple and the charge-exchange current vanishes within a pp pair, so that the one- and two-nucleon currents are suppressed in those regions. The small number of nucleons involved makes possible kinematically complete experiments, and exact Faddeev ground-state wave functions, as well as exact wave functions for the continuum three-body final state at low energies (below the pion-production threshold), are available [6,7].

Although the calculations of the ^{3}He ground-state wave function have reached a high level of accuracy in reproducing the bound-state properties [6,7], the calculation of the continuum three-nucleon wave function is less developed at higher energy; a full treatment of the three-body photodisintegration of ^{3}He has been possible only at energies $E_\gamma \leqslant 300$ MeV. As the energy increases, the number of partial waves and open channels becomes very large and, so far, no calculations that are both exact and complete have been done in the GeV region. Not only would a very large computational effort be required to do so, but also a treatment of the absorptive part of the nucleon-nucleon interaction (coupling to other open channels that is not taken into account in potential-based calculations) should be implemented.

A different approach has been taken by Laget [3,8–11], who has employed a diagrammatic model for the evaluation of the contribution of one-, two-, and three-body mechanisms in the cross section for the photodisintegration of ^{3}He. Rather than relying on a partial-wave expansion, this approach relies on the evaluation of the dominant graphs whose amplitudes are related to one- and two-body elementary amplitudes. The parametrization of these elementary amplitudes incorporates absorptive effects due to the coupling with other channels, which become more and more important as the energy increases. The comparison of these model predictions with experimental data provides us with a good starting point to understand the nature of three-body interactions in ^{3}He for photon energies in the GeV region.

At stake is the link with three-body forces. In the ^{3}He ground state, three-body forces involve the exchange of virtual mesons between nucleons and the creation of virtual baryonic resonances. The incoming photon can couple to each of these charged particles. Below the pion-photoproduction threshold, all the particles remain virtual and the corresponding three-body meson-exchange currents (MEC) contribute only weakly to the cross section. When the photon energy increases above the various meson- or resonance-production thresholds, these virtual particles can become real—they can propagate on-shell [1]. The corresponding sequential scattering amplitudes are considerably enhanced and can dominate certain well defined parts of the phase space. Kinematically complete experiments allow one to isolate each of the dominant sequential rescattering amplitudes. They analytically reduce to three-body MEC at lower energy, and put constraints on the corresponding three-body current.
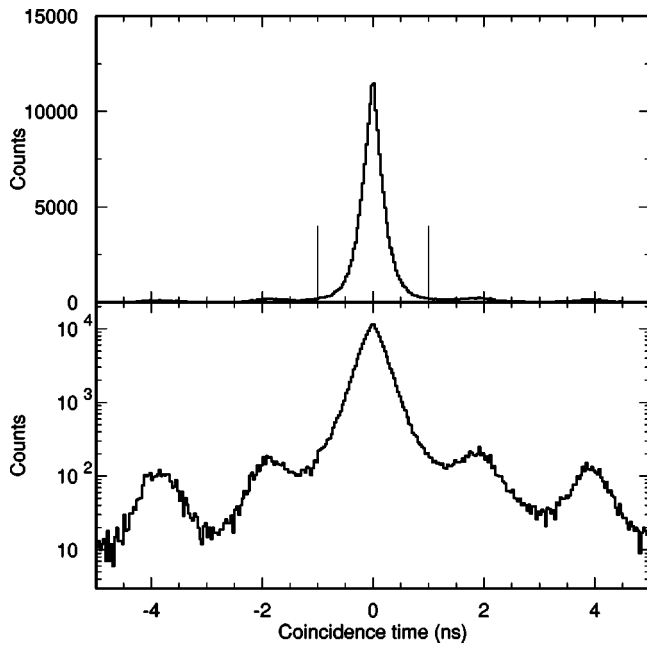

FIG. 1. Coincidence time for a subset of the raw data. The vertical lines in the upper panel indicate the time window for accepted events. Random coincidences from neighboring beam pulses are visible in the lower panel.
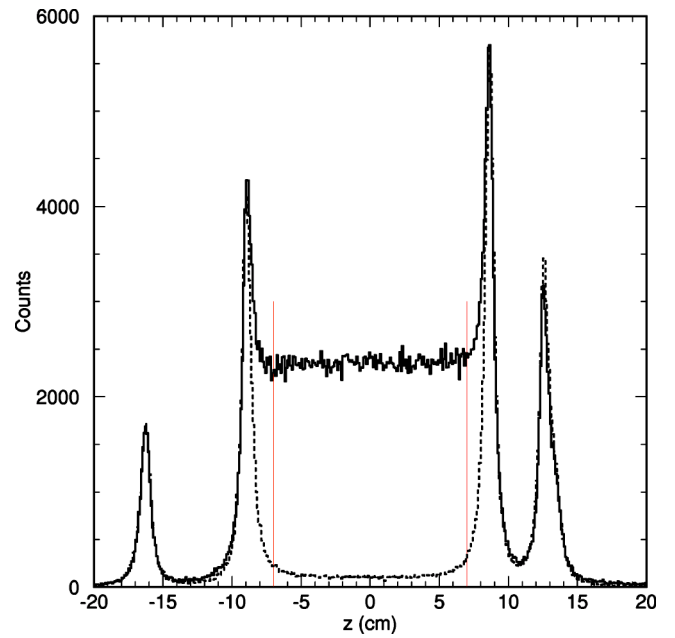

FIG. 3. Distribution of the z component (along the beam line) of the proton vertex. The solid line represents data obtained with a full target and the dashed line represents data taken with an empty target. The two inner peaks are events produced in the target walls, the two outer peaks represent protons produced in the superinsulation of the target cell and in its axial heat shield. The range -7 cm $< z < 7$ cm (vertical lines) has been chosen to select the pp events.

Several low-energy (<100 MeV) experiments have been performed since the publication of the results of the first measurement of the three-body photodisintegration of ^{3}He in 1964 [12], but only a few have been performed at intermediate photon energies up to 800 MeV, in limited kinematics [13–15] as well as with large-acceptance detectors [16–18]. They show good agreement with Laget's predictions provided that the $3N$ mechanisms, based on sequential pion ex-

FIG. 2. Velocity $\beta = v/c$ spectrum, as a function of particle momentum, for charged particles detected in the CLAS.

changes and Δ-resonance formation, are included in the calculations. Since these mechanisms dominate well defined parts of the phase space, a better understanding of the nature of many-body interactions requires one to perform a high-statistics full 4π investigation, probing the three-body breakup process for all angular and energy correlations of the three outgoing nucleons. Also, the extension to the high-energy ($E_\gamma \geq 1$ GeV) region, where no experiment has been performed until now, can be expected to open a window on other kinds of many-body processes.

This paper reports on a measurement of the three-body photodisintegration of ^{3}He performed in Hall B at Jefferson Lab [19]. Photon energies between 0.35 GeV and 1.55 GeV were used, and wide angular and momentum ranges for the outgoing particles were covered. These features, along with the high statistics collected, allow us to select the most interesting two- and three-body processes, to compare their relative importance, and to determine their variation with photon energy.

The experimental setup is described briefly in Sec. II, the salient points of the data analysis in Sec. III, and the model calculation in Sec. IV. Our results for several kinematic regions are presented in detail and compared with the model calculation in Sec. V, and summarized in Sec. VI.

II. EXPERIMENTAL SETUP

The experiment was performed at the Thomas Jefferson National Accelerator Facility, in Hall B, using the CEBAF Large Acceptance Spectrometer (CLAS) [20] and the brems-
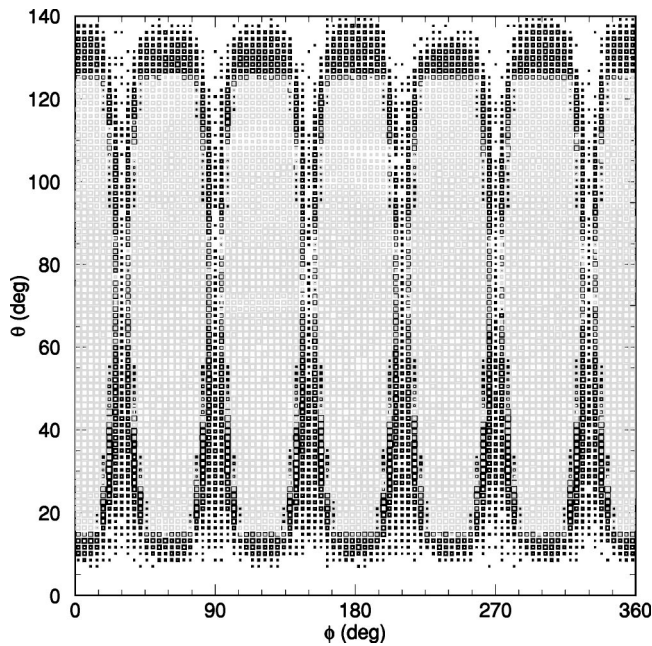
FIG. 4. Angular coverage for the identified protons. The gray areas represent the fiducial regions of the six CLAS sectors inside which the protons for the present analysis have been accepted.

FIG. 5. Missing mass of the $\gamma\,^3\mathrm{He}\to ppX$ system, for a subset of the selected pp events. One can easily distinguish the peak at the neutron mass at about 0.94 GeV/c^2 ($\sigma\sim0.017$ GeV/c^2) from the competing reaction channels.

strahlung photon tagger [21]. The electron beam energy was 1.645 GeV, corresponding to two passes of the CEBAF accelerator; the current was 10 nA during regular production runs and 0.1 nA during tagging-efficiency calibration runs. The photon beam was produced by the electron beam striking the radiator, a thin layer ($\sim5\times10^{-5}$ radiation length) of gold deposited on a thin carbon backing, which was placed 50 cm before the entrance of the tagger magnet. The electrons interacting in the radiator were deflected by the magnetic field of the tagging magnet, and those with energy between 20% and 95% of the incident electron beam energy were detected by two layers of scintillators (E-counters, measuring the energy of the electron, and T-counters, measuring its time [21]) placed in the magnet focal plane. Thus, photons in the energy range from 0.35 to 1.55 GeV were tagged. Two collimators were placed in the beamline between the tagger and the ^{3}He target, in order to eliminate the tails from the photon beam and to give a small and well defined beam spot on the target. The data were obtained using a cylindrical cryogenic target, 18 cm long and 4 cm in diameter, filled with liquid ^{3}He and positioned approximately 20 m downstream of the tagger radiator in the center of the CLAS. A lead-glass total absorption counter (TAC), almost 100% efficient, placed approximately 20 m downstream from the center of the CLAS detector, measured the tagging efficiency during low-flux calibration runs.

The CLAS is a magnetic toroidal spectrometer in which the magnetic field is generated by six superconducting coils. The six azimuthal sectors are individually equipped with drift chambers for track reconstruction, scintillation counters for time-of-flight measurement, Čerenkov counters for electron-pion discrimination, and electromagnetic calorimeters to identify electrons and neutrals. The polarization of the CLAS torus was set to bend the negatively charged par-
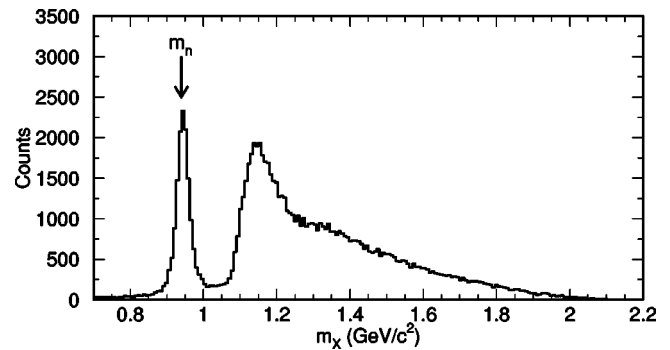
ticles toward the beam line. In order to achieve a good compromise between momentum resolution and negative-particle acceptance (required by other simultaneous experiments), the magnetic field of the CLAS was set to slightly less than half of its maximum value, corresponding to a torus current of 1920 A. A coincidence between the tagger and the time-of-flight scintillators defined the Level-1 trigger for accepting the hadronic events. For the first time in CLAS, a Level-2 trigger, which selected the events from among those passed through Level-1 that have at least one "likely track" in the drift chambers, was also used [20]. More than a billion events of production data were obtained with ^{3}He (plus a few
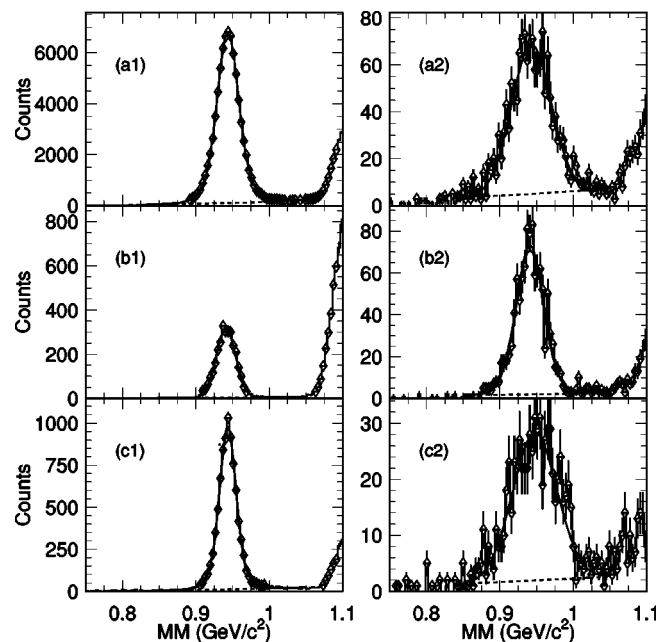

FIG. 6. Examples of missing-mass histograms fitted with a Gaussian curve plus an exponential (solid curve) for $0.43<E_\gamma<0.45$ GeV (a1) and $1.13<E_\gamma<1.15$ GeV (a2), for $0.08<p_n<0.10$ GeV/c and $0.45<E_\gamma<0.55$ GeV (b1) and $0.42<p_n<0.44$ GeV/c and $0.75<E_\gamma<0.85$ GeV (b2), and for $-0.88<\cos\theta_n<-0.84$ and $0.35<E_\gamma<0.45$ GeV (c1) and $0.72<\cos\theta_n<0.76$ and $0.95<E_\gamma<1.05$ GeV (c2). The background alone is shown as the dashed curves.
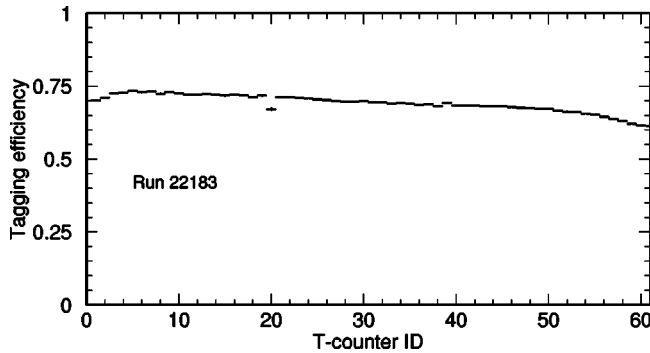
FIG. 7. Tagging efficiency as a function of T-counter number measured in one particular low-flux run. The average efficiency is about 70%.

million events taken with the target empty), at a data-acquisition rate slightly greater than 3 kHz.

III. DATA REDUCTION AND ANALYSIS

A. Channel identification

In order to isolate the ppn channel, a pp coincidence (with no other charged particles) in a time window of ±1 ns with a tagged photon defined the minimum condition for an accepted event, since the time interval between beam pulses is 2 ns. This coincidence time is shown in Fig. 1 for a subset of the raw data. The two protons were identified by their mass, deduced from their momentum measured in the drift chambers and their velocity measured with the time-of-flight scintillators, as shown in Fig. 2.

A cut on the interaction vertex, based on the analysis of empty-target runs, was performed to eliminate the background from pp events originating outside the target volume. Eliminating the events having the z component (where z is measured along the beam line) of the vertex more than 7 cm away from the center of the target, as shown in Fig. 3, reduced this background to less than 1% [19].

The particle-detection efficiency of the CLAS is not uniform and constant throughout its volume. At the edges of the active regions, delimited by the shadows of the six superconducting coils, the acceptance decreases and varies rapidly. In order to avoid errors, including poorly reconstructed tracks in the low-acceptance regions, a set of fiducial cuts, empirically determined, has been applied both to the momenta (p_1, $p_2 > 300$ MeV/c, $p \sim 300$ MeV/c being the CLAS detection threshold for protons) and to the polar and azimuthal angles (θ, ϕ) of the protons. The requirement of having the two protons in two different sectors of CLAS has also been applied, in order to avoid inefficiencies in the reconstruction of close tracks. The angular coverage for the accepted protons is shown in the light gray areas of Fig. 4.

Since the photon energy and the four-momenta of the two detected protons are known, and thus the ppn kinematics is completely determined, a missing-mass analysis can be performed to identify the neutron. Figure 5 shows the missing-mass distribution of the system $\gamma\,^3\text{He}\rightarrow ppX$. The first peak corresponds to the missing neutron, the second one to the

TABLE I. Systematic uncertainties in the measured cross sections. The total is the sum in quadrature of the individual uncertainties.

Quantity	Uncertainty %
Target length and density	2
Background subtraction	2
Detection efficiency	5
Photon flux	6
Total	8

other competing reaction channels, such as those producing pions which had not been detected by the CLAS, e.g., $\gamma\,^3\text{He}\rightarrow pp(n\pi^0)$ or $\gamma\,^3\text{He}\rightarrow pp(p\pi^-)$. About 25% of the two-proton events, ~5 million events, are thus identified as belonging to the ppn channel.

The momentum of each detected proton was corrected for its loss of energy while passing through the cryogenic target material, the target walls, the carbon-fiber scattering chamber, and the start-counter scintillators.

B. Background subtraction

After channel identification, the data were binned in photon energy, particle momentum, and particle angle. For each of these bins, a histogram of the two-proton missing-mass distribution was accumulated. Each pp missing-mass histogram was fitted with a Gaussian curve plus an exponential in order to reproduce the neutron peak and the background underneath it. The background is due both to misidentified or badly reconstructed protons and to the tail from competing reaction channels (see Fig. 5). Once the parameters of the fit are extracted, the yield is given by the area under the Gaussian curve. In this way, the contribution of the background is excluded. Some examples of the quality of these fits for various bins in photon energy, neutron momentum, and neutron angle, chosen to be typical of the character of the data for various conditions, are shown in Fig. 6. The background-to-signal ratio varies from less than 1% to 8%, depending on the kinematics.

To estimate the systematic uncertainty introduced by the fitting procedure used to subtract the background from the pp missing mass, the yields obtained with two kinds of fitting functions for the background (exponential and polynomial) have been compared with each other [19]. The deviations are, on average, of the order of 2%.

C. Efficiency

Since the neutron is reconstructed using the missing-mass technique, the detection efficiency for this channel is given by the probability of correctly detecting and identifying two protons in the CLAS. This has been evaluated with the aid of a Monte Carlo simulation. The ppn events, generated according to the three-body phase-space distribution, were processed by a GEANT-based code simulating the response of the CLAS, and were reconstructed and analyzed using the same
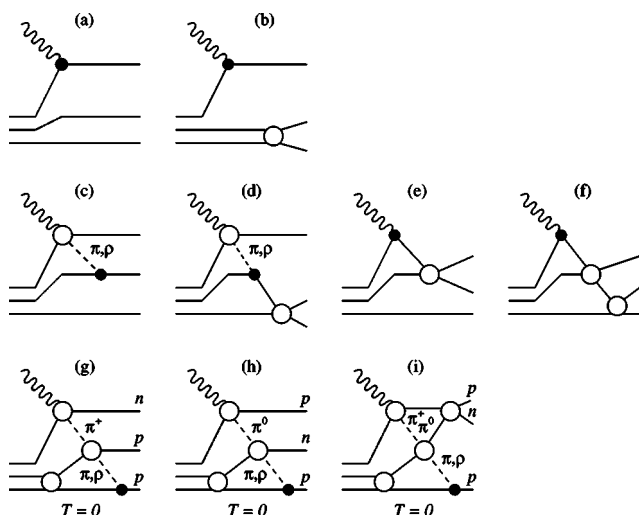
FIG. 8. Diagrams used in Laget's model [3,8–11] in the calculation of the ^{3}He$(\gamma,pp)n$ cross sections: (a) 1N absorption mechanism; (b) 1N+final state interactions (FSI); (c) 2N absorption; (d), (e), and (f) 2N+FSI; (g) and (h) 3N mechanisms; and (i) 3N+FSI. The open circles represent full transition amplitudes (T matrices); the filled circles are γNN and πNN Born terms.

procedure adopted for the experimental data. The efficiency inside the CLAS fiducial region for a given kinematical bin $\Delta\tau$ is defined as

$$\varepsilon(\Delta\tau)=\frac{N_r}{N_0}, \qquad (1)$$

where $\Delta\tau$ lies inside of the CLAS fiducial region, N_r is the number of reconstructed events within $\Delta\tau$, and N_0 is the number of events generated within $\Delta\tau$. The efficiency so computed is more or less constant as a function of photon energy, momentum, and angles, and its average value is slightly less than 95%.

In order to evaluate the systematic uncertainties in the efficiency for detecting the *ppn* events in the CLAS, the results obtained with the phase-space distribution have been compared with the efficiency computed with three other event distributions [19]. The result of the calculations of the efficiency inside of the CLAS fiducial region turns out to be independent of the model used to simulate the reaction, apart from the effect of bin migration due to the finite resolution of the detector, which has been found to be small. The resulting systematic uncertainty was determined to be no greater than 5% [19].

D. Cross sections and normalization

Three kinds of CLAS-integrated cross sections have been measured and are reported here. They are (i) total cross sections, defined as

$$\sigma=\frac{N_{ppn}}{L\varepsilon}; \qquad (2)$$

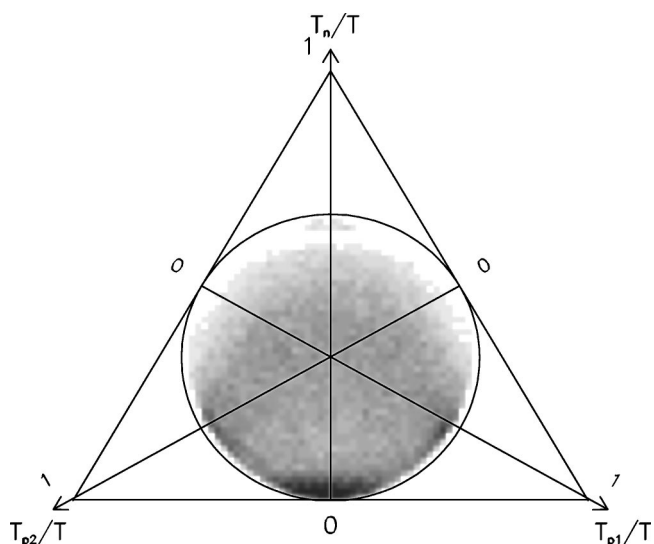(ii) semidifferential cross sections with respect to momentum, defined as

FIG. 9. Triangular Dalitz plot for the *ppn* data. T_{p1}, T_{p2}, and T_n are the center-of-mass kinetic energies of the three nucleons.

$$\frac{d\sigma}{dp}=\frac{N_{ppn}}{\Delta pL\varepsilon}; \qquad (3)$$

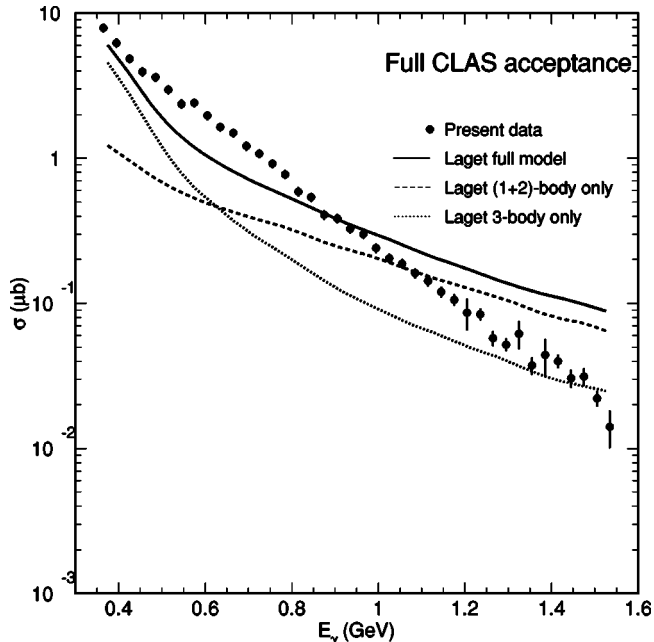and (iii) semidifferential cross sections with respect to $\cos\theta$, defined as

FIG. 10. Total *ppn* cross section integrated over the CLAS acceptance plotted as a function of photon energy on a logarithmic scale for the full E_γ range. The *ppn* cross section (circles) is compared with Laget's full model (solid curve), with the model result without the three-body mechanisms (dashed curve), and with the one including only three-body processes (dotted curve). The error bars include statistical and systematic uncertainties, as in all the following experimental distributions.
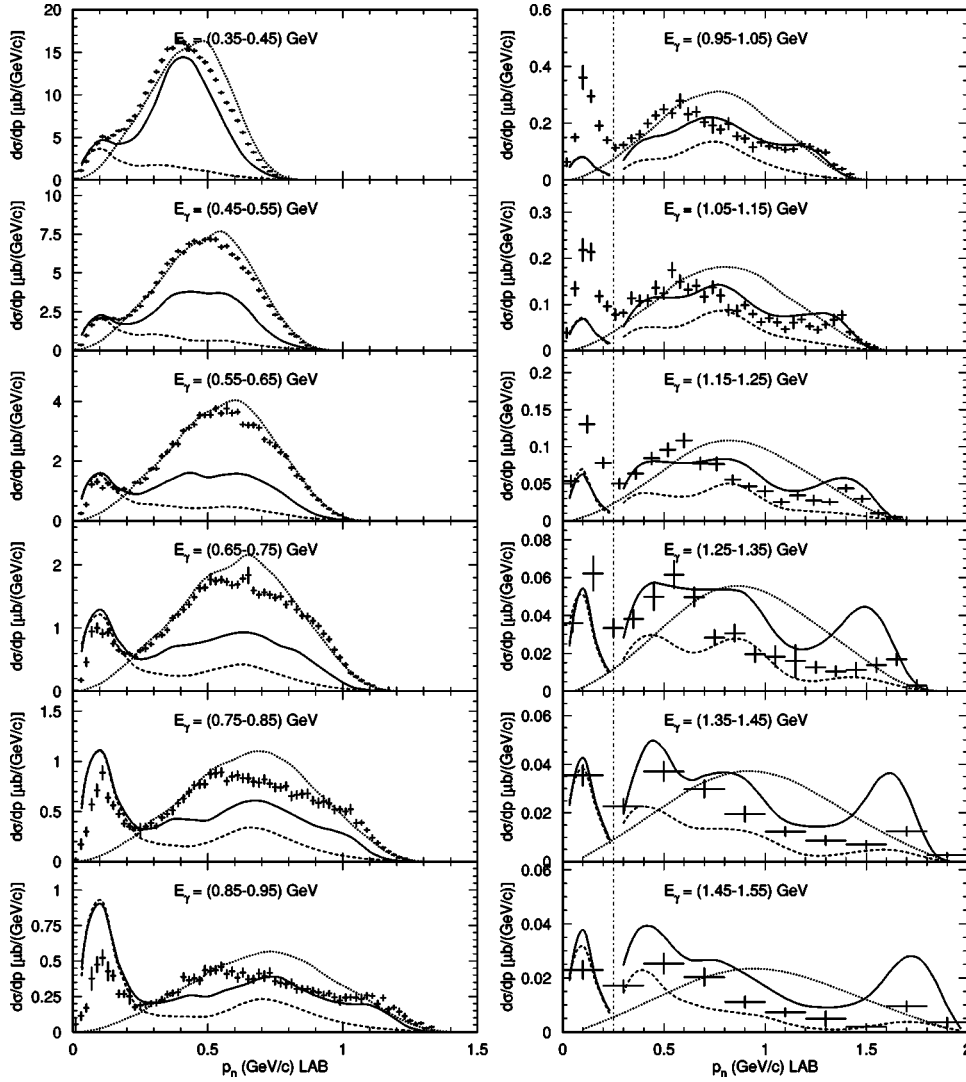
FIG. 11. Differential cross sections integrated over the CLAS as a function of the neutron momentum in the laboratory frame for 12 0.1-GeV-wide photon-energy bins between 0.35 GeV and 1.55 GeV. The points represent our CLAS data. The error bars include both statistical and systematic uncertainties. The dotted curves are the distributions for phase-space events generated within the CLAS acceptance and normalized in each energy bin to match the total area of each experimental distribution. The solid curves represent the full Laget-model results, while the dashed lines represent the model including one- and two-body mechanisms only. For $E_\gamma > 0.95$ GeV, the model predictions at $p_n < 250$ MeV/c (to the left of the vertical dotted-dashed line) are scaled by a factor 0.1 to fit in the plots.

$$\frac{d\sigma}{d\Omega} = \frac{N_{ppn}}{2\pi\Delta(\cos\theta)L\varepsilon}, \qquad (4)$$

where N_{ppn} is the number of events in the bin, ε is the detection efficiency defined in Sec. III C, and L is the luminosity, which is defined as

$$L = N_\gamma \frac{\rho z N_A}{A}, \qquad (5)$$

where $\rho = 0.0675$ g/cm^3 is the density of the target, $z = 14.0$ cm is the effective target length, A is the atomic mass of the target ($A = 3.016$ g/mol), N_A is Avogadro's number, and N_γ is the number of incident photons.

The systematic uncertainties in the target length and density are of the order of 2%. The photon flux was measured by integrating the tagger rate over the data-acquisition lifetime. The tagging efficiency was measured during low-flux runs, using the lead-glass total absorption detector. For each T-counter i, the tagging efficiency is defined as [21]

$$T_{eff}(i) = (T_i \cdot TAC)/T_i^{raw}, \qquad (6)$$

where $T_i \cdot TAC$ is the rate of coincidences between tagger and total absorption counter, and T_i^{raw} is the rate in the tagger alone. A typical tagging efficiency spectrum, as a function of T-counter number, is shown in Fig. 7.

To estimate the systematic uncertainty for the photon flux, the variations with time of the tagging efficiency and of the proton yield normalized to the photon flux for each tagger scintillation counter have been studied. The resulting systematic uncertainty is, on average, approximately 6% [19]. The values of the systematic uncertainties in the measured cross sections are summarized in Table I. The luminosity, integrated over the entire running time and over the full photon-energy range, was $L \simeq 8.7 \times 10^{35}$ cm^{-2} for this experiment.

IV. MODEL CALCULATION

As mentioned in the Introduction, the only theoretical model currently available for calculation of the cross section for the three-body photodisintegration of ^{3}He in the GeV energy region is the one by Laget. In this model, the fivefold differential cross section in the laboratory system for the
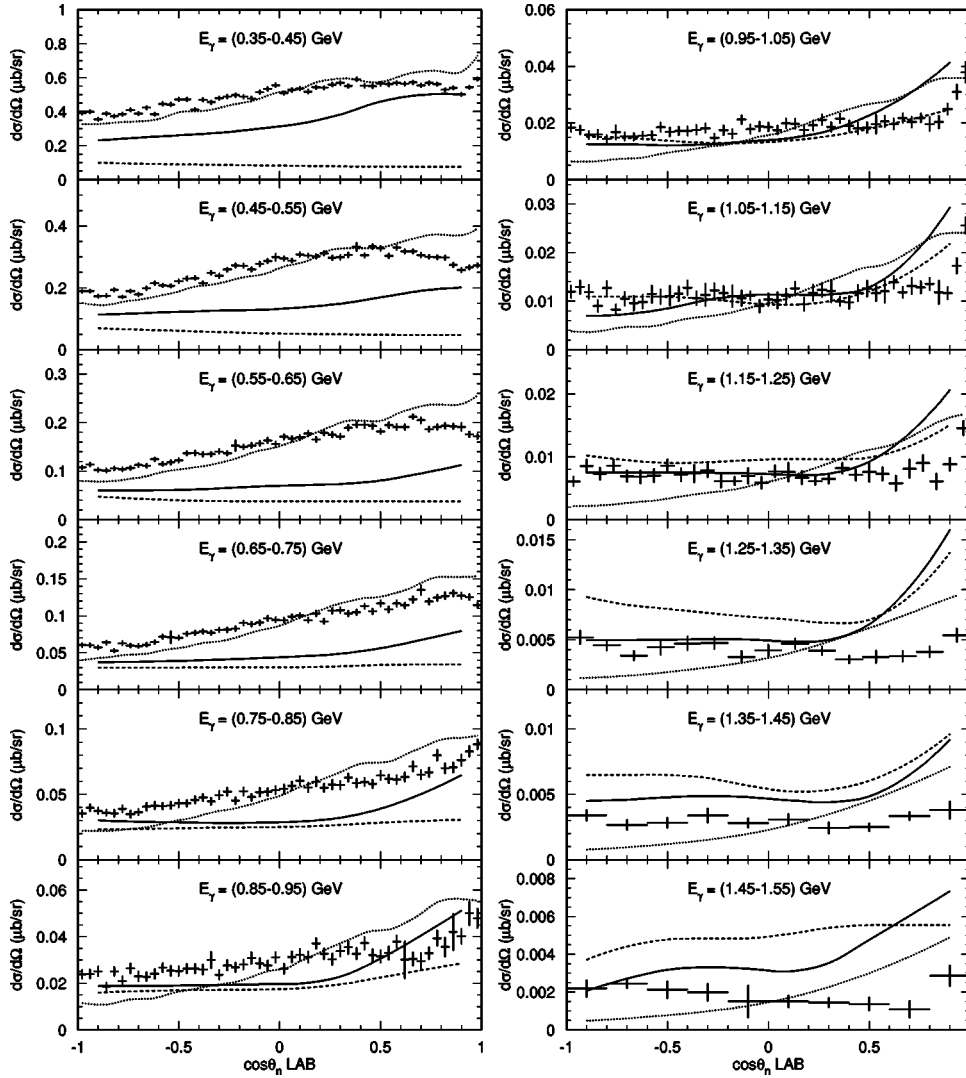
FIG. 12. Differential cross sections integrated over the CLAS as a function of the cosine of the neutron polar angle in the laboratory frame for 12 0.1-GeV-wide photon-energy bins between 0.35 GeV and 1.55 GeV. The points represent our CLAS data. The error bars include statistical and systematic uncertainties. The dotted curves are the distributions for phase-space events generated within the CLAS acceptance and normalized in each energy bin to match the total area of each experimental distribution. The solid curves represent the full model results, while the dashed lines represent the model including one- and two-body mechanisms only.

$\gamma\,^3\mathrm{He} \rightarrow ppn$ reaction is connected through a Jacobian to a *reduced cross section,*

$$\frac{d^5\sigma}{dpd\Omega_1 d\Omega_2} = \frac{E_n p_2^3 p_1^2}{E_1 p_n^2 |E_n p_2^2 - E_2 \vec{p}_n \cdot \vec{p}_2|} \left(\frac{Q}{p}\right)_{cm}$$
$$\times \frac{d^5\sigma_{red}}{(d\Omega_1)_{cm} dp_n d\Omega_n}, \qquad (7)$$

where $(E_1, \vec{p}_1)$, $(E_2, \vec{p}_2)$, and $(E_n, \vec{p}_n)$ are, respectively, the four-momenta of the two outgoing protons (1 and 2) and the neutron in the laboratory frame, and p and Q are the proton momentum and the total energy measured in the center-of-mass frame of the two protons.

The reduced cross section depends on the transition amplitude $\mathrm{T}(\gamma\,^3\mathrm{He} \rightarrow ppn)$ [4,5],

$$\frac{d^5\sigma_{red}}{(d\Omega_1)_{cm} dp_n d\Omega_n} \propto |\langle \Psi_{ppn} | T | \Psi_{^3\mathrm{He}} \rangle|^2. \qquad (8)$$

The fully antisymmetrized $^3\mathrm{He}$ bound-state wave function $|\Psi_{^3\mathrm{He}}\rangle$ is the solution of the Faddeev equations [22] for the Paris potential [23]. It is expanded in a basis where two nucleons couple to angular momentum L, spin S, and isospin T, the third nucleon moving with angular momentum l. Each component is approximated by the product of the wave functions, which describe the relative motion of the two nucleons inside the pair and the motion of the third nucleon [24]. Fermi-motion effects are taken fully into account in the two-body matrix element, and partially [3] in the three-body matrix element. However, it has been ascertained that the effect of the Fermi motion in the three-body matrix element does not significantly affect the results; therefore, it has not been implemented in the version of the model which has been used here with the Monte Carlo procedure in order to avoid prohibitive computation time. All of the S, P, and D components of the $^3\mathrm{He}$ wave function are included. The energy and momentum are conserved at each vertex, and the kinematics is relativistic. The continuum final state $|\Psi_{ppn}\rangle$ is approximated by a sum of three-body plane waves and half-off-shell amplitudes (which are the solutions of the Lippman-Schwinger equation for the Paris potential) where two nucleons scatter, the third being a spectator. Only S-wave NN scattering amplitudes have been retained in the version used in this work. The antisymmetry of the continuum final state is achieved by exchanging the roles of the three nucleons [10]. The transition amplitude T is expanded in a truncated

series of diagrams that are thought to be dominant. These diagrams, that were thought to include the most likely one-, two-, and three-body mechanisms, are computed in momentum space. Among all the possible three-body mechanisms, meson double scattering is the most likely to occur. The Feynman diagrams included in the present version of the model are shown in Fig. 8. The open circles represent the full transition amplitudes (T matrices), which have been calibrated against the corresponding elementary channels, and the filled circles are just the γNN and πNN Born terms.

The first two diagrams, (a) and (b), describe one-body photoabsorption; (c), (d), (e), and (f) represent two-body processes [25,26]; and (g), (h), and (i) are three-body mechanisms, with two-meson (π or ρ) exchange. Pion absorption by a $T=1$ (pn or pp) pair has been found experimentally to be strongly suppressed [27], at least at low energies, and has not been included in the model at this stage. The $3N$ absorption mechanism shown in diagram (g) represents the primary $3N$ process for the $^3\mathrm{He}(\gamma,pp)n$ reaction. Above the photon energy corresponding to the pion-production threshold, the calculation does not contain any free parameters, since all of the basic matrix elements have been fixed independently using relevant reactions induced on the nucleon and on the deuteron [4,5]. The calculated cross section involves a logarithmic singularity associated with the on-shell propagation of the "first" exchanged pion, which shows up, and moves when the photon energy varies, in a well defined part of the phase space. Below the pion threshold, both exchanged pions are off their mass shells, and the three-body exchange currents can be linked by gauge invariance to the corresponding three-body forces [3,8–11].

All model calculations discussed in the following sections have been performed with Monte Carlo sampling over the CLAS geometry to produce cross sections that can be compared with the experimental results. The small-scale structures which are seen in some of the model results result from this Monte Carlo treatment, although the major structures are real features of the model calculations.

V. RESULTS

A. Cross sections integrated over CLAS

The use of a triangular Dalitz plot is very suitable to look for the deviations of an experimental distribution from pure phase-space predictions and to identify correlations between three final-state particles. In particular, this technique can be used to identify and select the regions of the phase space where three-body processes can be dominant. If T_{p1}, T_{p2}, and T_n are the center-of-mass kinetic energies of the two protons and the neutron, respectively, and T is their sum, we can define the Cartesian coordinates of the triangular Dalitz plot as

$$x = \frac{1}{\sqrt{3}} \frac{T_{p1} - T_{p2}}{T} \quad \text{and} \quad y = \frac{T_n}{T}.$$

Figure 9 shows the distribution of the ppn events on the Dalitz plot after applying the selection cuts. The wide acceptance of the CLAS allows us to fill the physically accessible
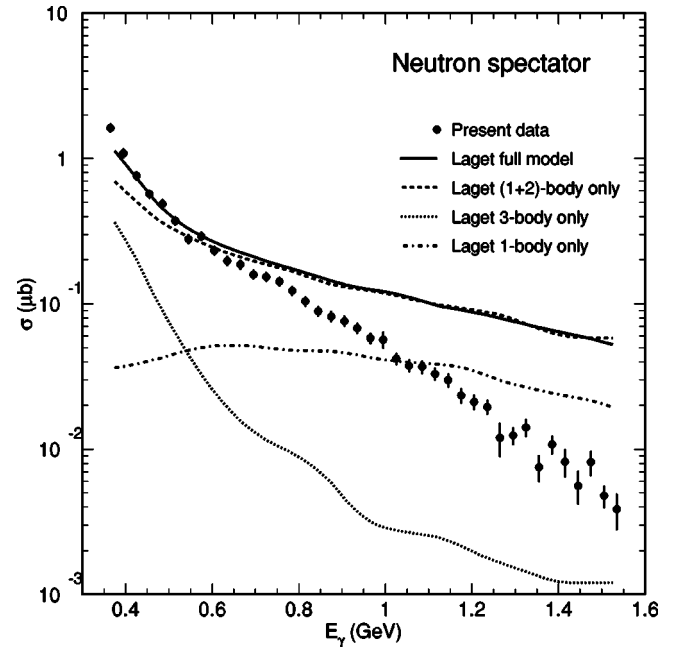

FIG. 13. Cross section integ rated over the CLAS for the neutron-spectator kinematics plotted as a function of photon energy. The data are compared with the predictions of the full model (solid curve), the (1+2)-body part (dashed curve), the three-body part (dotted curve), and the one-body part alone (dashed-dotted curve).

region—delimited by the boundary circle—almost completely.

The shading of the boxes indicates the yield of the observed ppn events. Areas of increased yield are visible where the T_{p1} and T_{p2} axes intercept the boundary circle, as well as where $T_n \approx 0$. These areas correspond to quasi-two-body breakup and neutron-spectator kinematics, respectively; they are discussed in detail in Secs. V A 4 and V A 2 below. The depletion areas in the upper left and upper right sides of the circle correspond to the kinematics where one of the protons has low momentum ($p_1, p_2 < 300$ MeV/c) and therefore is not detected by the CLAS. The central top area where the two protons are emitted in nearly the same direction is excluded by the requirement of detecting the two protons in two different sectors (see Sec. III A above). The central region, near the intersection of the three axes, consists of events where all three nucleons have nearly equal energies, and is called the "star" region (see Sec. V A 3 below).

In the following sections, CLAS-integrated cross sections for the full acceptance and for the three selected kinematics listed above, each chosen to illustrate its two-body or three-body character, are presented and compared with distributions obtained both with three-body phase space and with the results of the Laget model.

1. Full CLAS acceptance

The ppn total cross section integrated over the CLAS acceptance has been measured as a function of the incident photon energy E_γ. The photon-energy spectrum, ranging from 0.35 GeV to 1.55 GeV, has been divided into 60 bins, each 0.02 GeV wide. The results are shown in Fig. 10. The
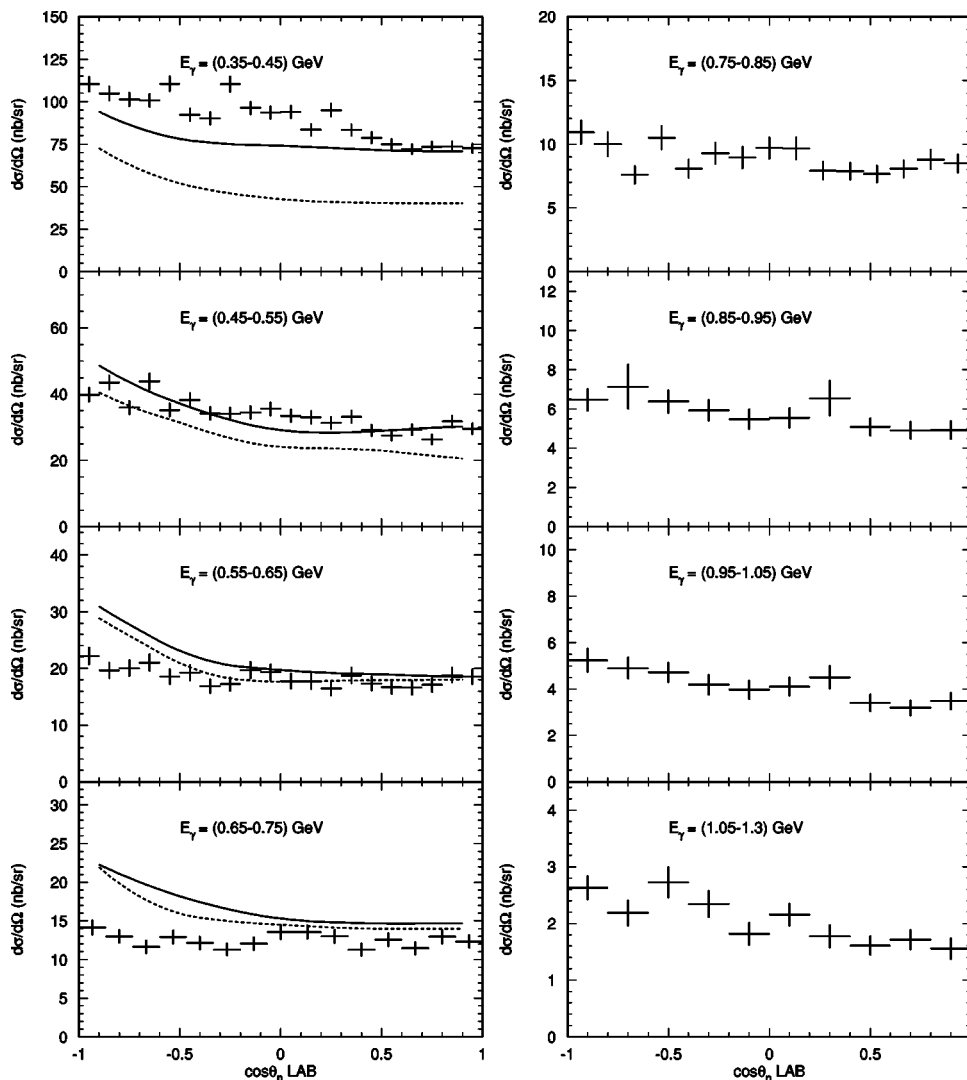
FIG. 14. Differential cross sections integrated over the CLAS for the neutron-spectator kinematics with respect to $\cos\theta$ of the neutron in the laboratory frame for photon energies between 0.35 and 1.30 GeV. The data are compared with the results of the full model (solid curves) and those of the one- plus two-body-only model (dashed curves), for $0.35 < E_\gamma < 0.75$ GeV only, because at higher energies the model calculations differ by more than an order of magnitude from the data.

cross section, ranging between 10 μb and 0.01 μb, decreases almost exponentially as the photon energy increases. Fitting the data with an exponential function $\sigma(E_\gamma) \propto e^{-bE_\gamma}$ yields a slope $b \simeq 5.3$ GeV^{-1}. The data are compared with the full calculation (solid curve), including one-, two-, and three-body mechanisms, as well as with the results for the one- and two-body mechanisms only (dashed curve), and the three-body mechanisms only (dotted curve), as shown in Fig. 8. It is important to note that the theoretical curves represent *absolute cross sections* calculated within the CLAS acceptance—they are not normalized to the data. The results of the model calculations that do not include the three-body mechanisms are almost a factor of 10 smaller than the data at lower energies, while they approach the data as the photon energy increases and exceed the data at higher energies. The full-model results agree better with the data, but still are too low at low energies and too high at high energies.

Figure 11 shows the partial differential cross section as a function of neutron momentum p_n, for 12 0.1-GeV-wide photon energy bins. The data are compared with phase-space-generated event distributions (dotted curves) normalized in each energy bin in order to match the area under the experimental distribution, with the results of Laget's full

model (solid curve), and with the model with no three-body mechanisms included (dashed curve). The neutron momentum distributions are related to the projection of the data in Fig. 9 onto the T_n axis.

In the photon-energy range between 0.35 and 0.95 GeV, the data show a broad central distribution in the middle of the neutron momentum spectrum (e.g., at about 400 MeV/c for $E_\gamma = 0.4$ GeV and 500 MeV/c for $E_\gamma > 0.5$ GeV), which is reproduced reasonably well by the phase-space distribution (better at low photon energies than at high energies). Up to about 0.6 GeV, a comparison of the data with the shape of the model results reveals the presence of three-body mechanisms. In the middle range of neutron momentum, two-body mechanisms are seen to contribute increasingly starting from $E_\gamma = 0.65$ GeV. These contributions stem from low-energy S-wave np rescattering, which causes the increased yield in the quasi-two-body kinematics, corresponding to the left and right sides of the Dalitz plot (Fig. 9). This yield projects onto the middle range of the neutron-momentum distribution.

A peak, roughly 0.04 GeV/c wide, is observed at a neutron momentum of about 0.12 GeV/c, independent of the photon energy. The relative strength of this peak increases with increasing photon energy, but it is not accounted for by
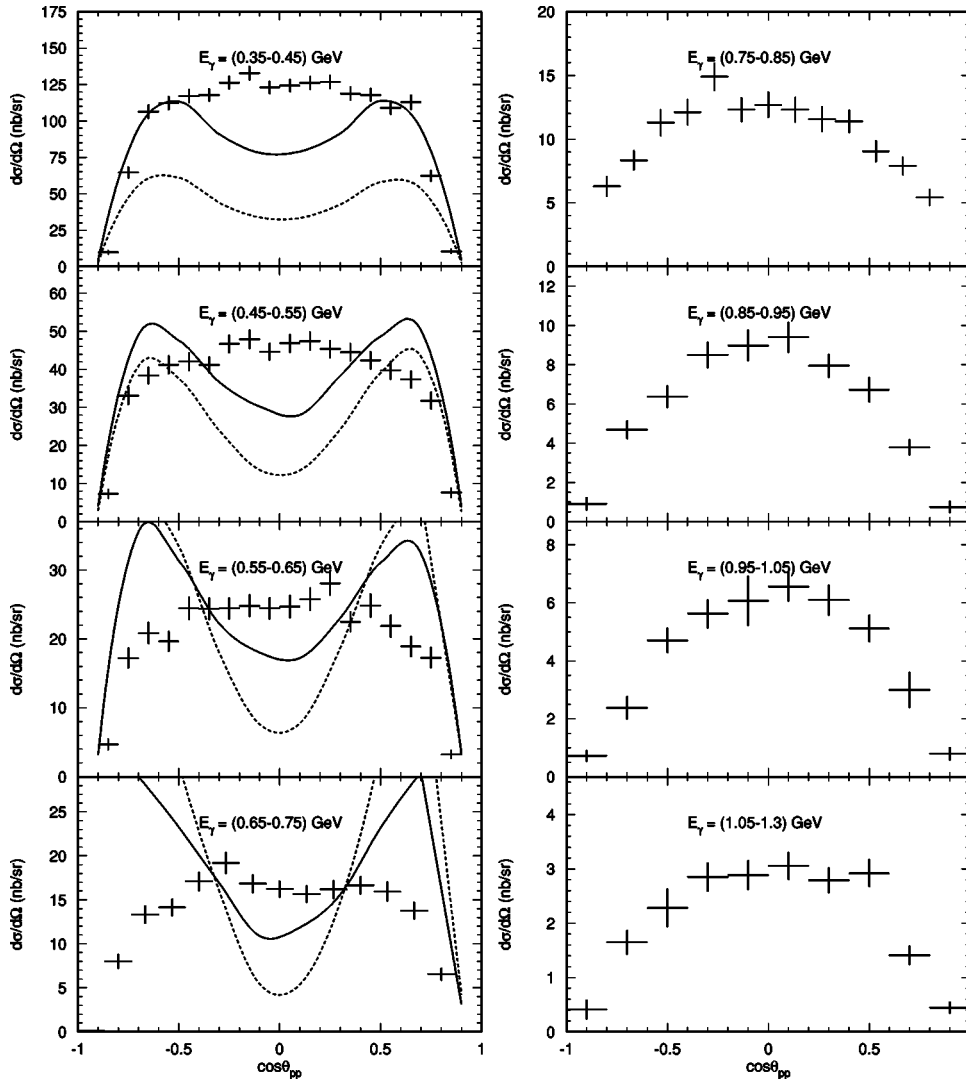
FIG. 15. Differential cross sections integrated over the CLAS for the neutron-spectator kinematics with respect to $\cos\theta_{pp}$ of the proton in the pp-pair center-of-mass frame for photon energies between 0.35 and 1.30 GeV. The data are compared with the results of the full model (solid curves), and those of the one- plus two-body-only model (dashed curves), for $0.35 < E_\gamma < 0.75$ GeV, because at higher energies the model calculations differ by more than an order of magnitude from the data.

the three-body phase-space distribution. However, this structure is expected by the model, and it is predicted to be largely due to two-body mechanisms. It reflects the Fermi distribution of the spectator neutron. This feature has been exploited to select the neutron-spectator kinematic region, as is explained in Sec. V A 2 below.

At photon energies from about 0.9 to 1.2 GeV and high neutron momenta, a third structure appears in the data, which is present neither in the phase-space distribution nor in the $(1+2)$-body model results, but is predicted by the full model. This structure can therefore be considered to be a signature of three-body mechanisms as well.

The differential cross section as a function of the cosine of the neutron polar angle $\cos\theta_n$ in the lab system is plotted in Fig. 12, for 12 0.1-GeV-wide photon-energy bins, between 0.35 GeV and 1.55 GeV. The distributions are forward-peaked at low-to-intermediate energies, while they become flatter for higher E_γ. Their shapes are reasonably well reproduced by both phase-space and the full-model calculations.

2. Spectator neutron

Guided by Fig. 11, the events where the neutron is a spectator in the photobreakup of a proton pair have been selected

by requiring the condition $p_n < 250$ MeV/c. These are all the events in the lower neutron-momentum peak (within 3σ from its center).

Figure 13 shows the cross section as a function of photon energy integrated over the CLAS for the events satisfying this condition, compared with the predictions of the model. After an initial steep drop, the cross section has an exponential dependence on the photon energy above 0.6 GeV, this
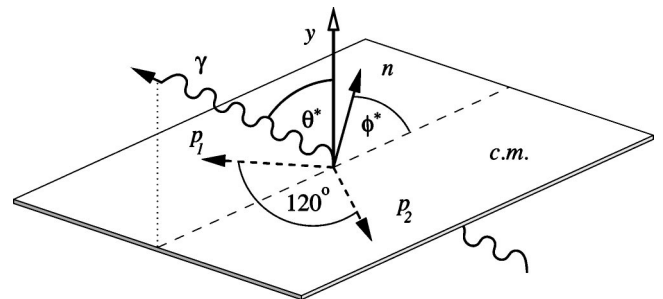

FIG. 16. Kinematics of the star configuration in the ppn center-of-mass frame. The angles θ^*, between the normal vector to the star plane and the photon-beam direction, and ϕ^*, the neutron azimuthal angle in the star plane, define the reaction.

time with a slope $b \simeq 4$ GeV^{-1}. The agreement between the experimental cross section and the model prediction is good only for low energies, below 600 MeV. The cross section is clearly driven by two-body mechanisms, as expected.

The differential cross section as a function of $(\cos \theta_n)_{lab}$, which is plotted in Fig. 14 for eight photon-energy bins, shows a generally flat distribution. This is expected, because in the neutron-spectator kinematics the two-body part of the reduced differential cross section is proportional to the neutron-momentum distribution $\rho(n)$ times the center-of-mass differential cross section for the *pp*-pair breakup [8],

$$\frac{d\sigma_{red}}{d\Omega_{cm}d\vec{p}_n} = (1 + \beta_n \cos \theta_n)\rho(p_n)\frac{d\sigma}{d\Omega_{cm}}(\gamma pp \rightarrow pp). \quad (9)$$

Both the (1+2)-body part and the full-model results agree fairly well, in shape and magnitude, with the experimental distributions up to 600 MeV. At higher energies, the calculation predicts the contribution of two-body mechanisms to be much too large.

In the neutron-spectator kinematics, the primary physics is contained in the angular distribution of the $\gamma pp \rightarrow pp$ subchannel. Figure 15 compares this angular distribution with the model. While the magnitude of the experimental cross section is well reproduced at low energy by the model, the shape of the angular distribution is markedly different. The model curve exhibits a minimum at 90°, where the measured differential cross section has a broad maximum. It can be seen from Fig. 13 that three-body diagrams do not contribute significantly to the total cross section, but their interference with the two-body diagrams brings the shape of the angular distributions closer to the experimental ones. However, this effect is not strong enough to cancel the huge contribution of the two-body part at high energy.

Since the *pp* pair that absorbs the photon has no dipole moment for the photon to couple with, charged-meson exchange currents and intermediate-Δ production [Fig. 8, diagrams (c) and (d)] are strongly suppressed and one-body mechanisms [diagrams (a) and (b)] and related FSI [diagrams (e) and (f)] contribute more significantly to the two-body photodisintegration cross section $(d\sigma/d\Omega)(\gamma pp \rightarrow pp)$. At low energy, the one-body amplitude is driven by dipole photon absorption, which is suppressed. At high energy, it involves all other multipoles and, as a result, the corresponding cross section remains almost constant. This process probes the relative *pp* wave function at a momentum which increases with the incoming photon energy—typically 400 MeV/c at $E_\gamma = 400$ MeV, increasing to 1.5 GeV/c at $E_\gamma = 1.2$ GeV. Above ~ 0.8 GeV, the *pp* wave function is not under control, and we are reaching the limits of the model, as in the $\gamma d \rightarrow pn$ reaction [28]. We may have entered a region where quarks become the relevant degrees of freedom [28,29], or perhaps a description in terms of Regge-type calculations [30] is more suitable.

3. Star configuration

The center of the Dalitz triangle corresponds to the three particles having equal kinetic energies and their three-momentum vectors forming angles of 120° with each other
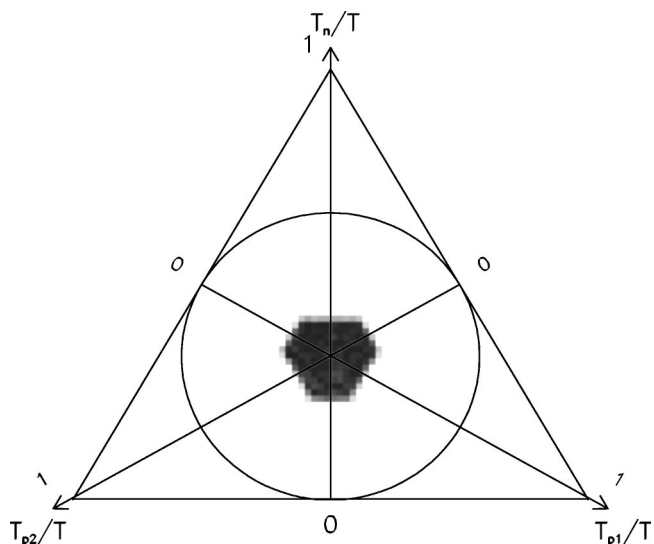

FIG. 17. Dalitz plot for the CLAS *ppn* events selected for the *star configuration*.

(in the *ppn* center-of-mass frame). For this reason, this kinematical arrangement, shown schematically in Fig. 16, has been called the *star configuration*. In this region, the three-body mechanisms are expected to be dominant because if the momentum is equally shared between the three nucleons, the contribution from two-body mechanisms is minimized. This is therefore considered to be a good place to study three-body mechanisms.

The events for this kinematics have been selected by requiring that the three nucleons satisfy the condition
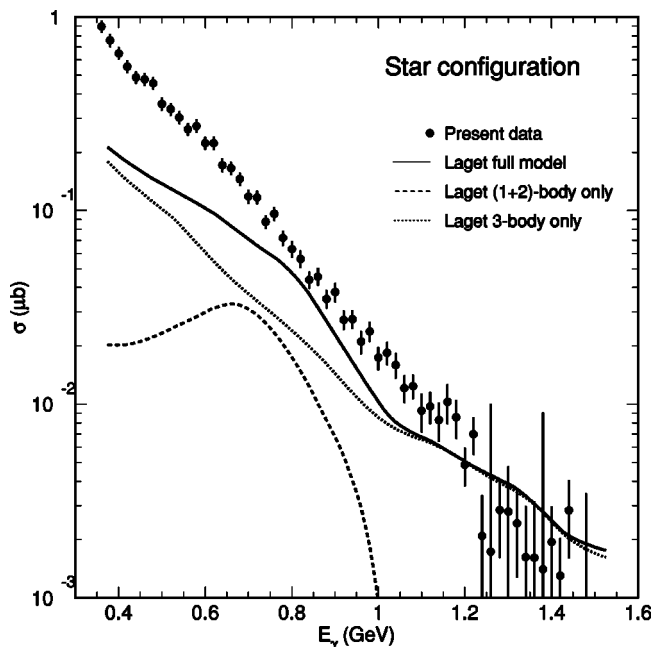

FIG. 18. Cross section integrated over the CLAS acceptance for the star configuration plotted as a function of incident photon energy. The CLAS data are compared with the predictions of the full model (solid curve), to the one- plus two-body-only part (dashed curve), and to the three-body-only part of the model (dotted curve).
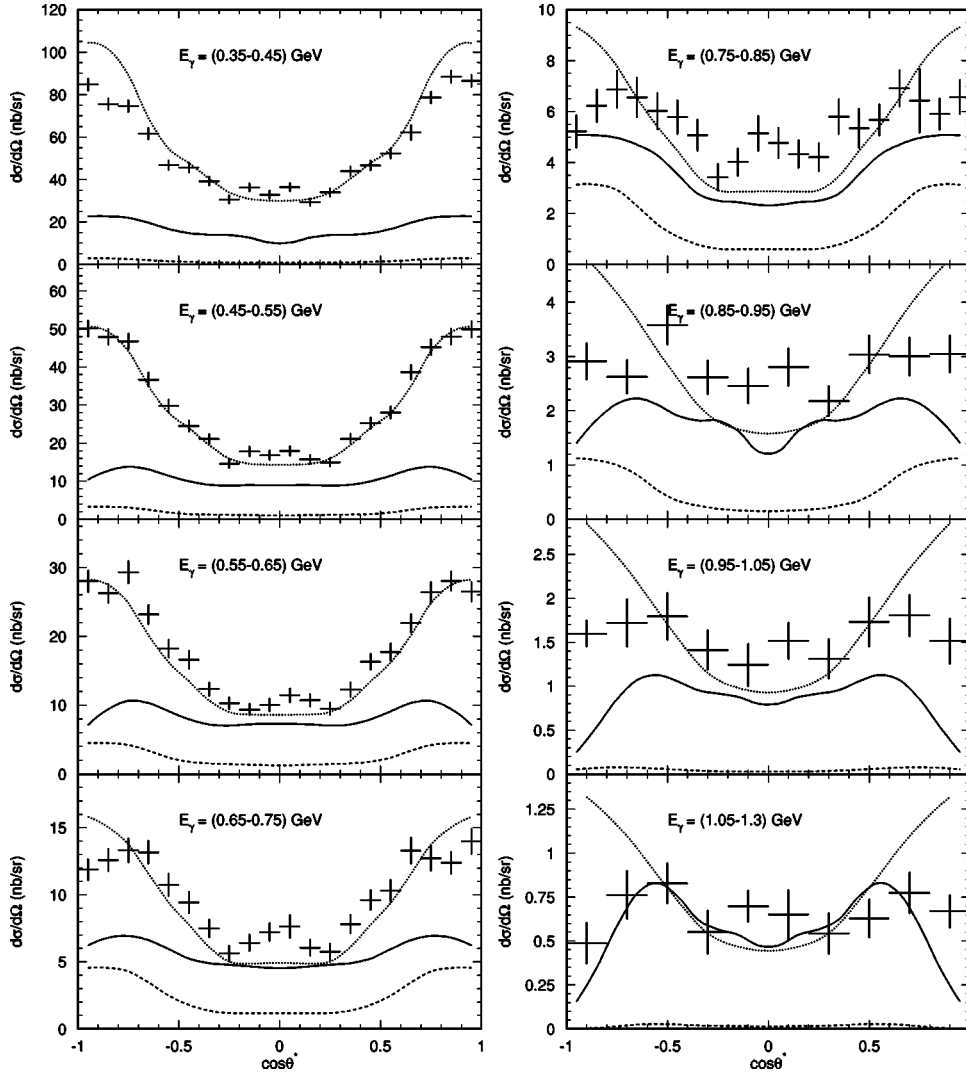
FIG. 19. CLAS-integrated differential cross sections with respect to $\cos \theta^*$ for the star configuration. The data, for photon energies between 0.35 and 1.30 GeV, are compared with the full-model results (solid curves) and the one- plus two-body-only part (dashed curves). The dotted curves are the phase-space distributions multiplied, for each photon-energy bin, by the constants used to normalize the full-Dalitz cross sections.

$$|\theta_{ij} - 120°| < \delta_\theta, \qquad (10)$$

where

$$\theta_{ij} = \arccos\left(\frac{\vec{p}_i \cdot \vec{p}_j}{p_i p_j}\right) \qquad (11)$$

is the angle between the momenta of nucleons i and j, in the center-of-mass frame, and the angle δ_θ, which expresses the allowed deviation from the pure "star" kinematics, has been chosen to be 15°, as shown in Fig. 17.

In Fig. 18, the cross section integrated over the CLAS for the star configuration is plotted as a function of photon energy. It decreases exponentially, with slope $b \simeq 5.8$ GeV^{-1}, as the photon energy increases, much more steeply than for the neutron-spectator kinematics.

As expected from the kinematics, for the star configuration the contribution of two-body mechanisms is negligible, while the bulk of the cross section comes from three-body mechanisms. At low energy, the model misses the experimental cross section by approximately a factor of 4. The probable reason for this discrepancy is that only the Born term and the Δ-formation term [31] have been retained in the

calculation of the $\gamma N \rightarrow \pi N$ vertex [the upper blob in Figs. 8(g) and 8(h)]. The addition of the contributions of the $N(1520)D_{13}$, $N(1440)P_{11}$, and $N(1535)S_{11}$ resonances also might improve the agreement with the data. At high E_γ, the Blomqvist-Laget Born term matches the Regge amplitudes [32] that reproduce the $\gamma N \rightarrow \pi N$ cross section in this energy region. The pion-rescattering amplitude [Figs. 8(g)–8(i)] is parametrized in terms of partial waves up to and including G-waves.

The differential cross section as a function of $\cos \theta^*$, the cosine of the angle between the incident photon and the normal vector to the three-nucleon center-of-mass plane (see Fig. 16), is plotted in Fig. 19 for eight photon-energy bins between 0.35 GeV and 1.30 GeV. Since the two outgoing protons are indistinguishable, the orientation of the normal vector to the star plane, $\vec{p}_1 \times \vec{p}_2$, is arbitrary. Thus, the distribution is symmetric around $\cos \theta^* = 0$. The shape of the cross section is very well reproduced by phase space at low energy, while at high energy the model better reproduces the curvature of the experimental distribution. At all energies, the three-body mechanisms are dominant.

Figure 20 shows, for eight photon-energy bins between 0.35 GeV and 1.30 GeV, the differential cross section as a
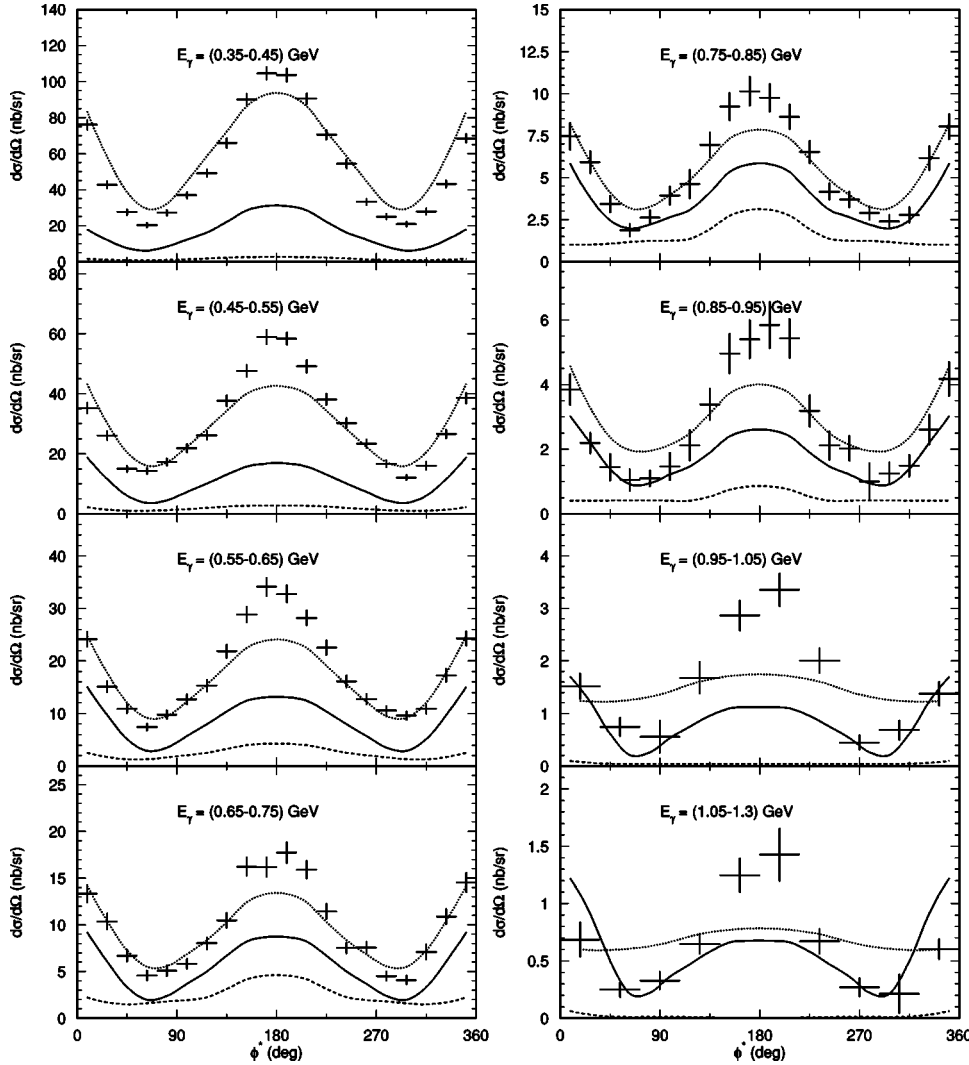
FIG. 20. CLAS-integrated differential cross sections with respect to ϕ^* for the star configuration. The data, for photon energies between 0.35 GeV and 1.30 GeV, are compared with the full-model results (solid curves) and the one-plus two-body-only part (dashed curves). The dotted curves are the phase-space distributions, multiplied, for each photon-energy bin, by the constants used to normalize the full-Dalitz cross sections.

function of the angle ϕ^* between the neutron direction in the star plane and the projection of the photon-beam direction in the same plane (see Fig. 16). As is the case for θ^*, the angular distribution is symmetric, here around 180°. It also follows a phase-space distribution, except for $E_\gamma > 0.95$ GeV, and its shape (but not its magnitude) is reproduced fairly well by the model as well. Again, three-body mechanisms are seen to be dominant.

The photoproduced pion described by the diagrams (g) and (h) of Fig. 8 can propagate on-shell, since the available energy is larger than the sum of the masses of the pion and the three nucleons. This causes the development of a logarithmic singularity in the three-nucleon amplitude, which should *enhance* the contribution of three-body mechanisms. The effect of this singularity can be seen in Fig. 21, in which is plotted the cross-section differential in m_X^2/m_π^2, where m_X, defined from the relation

$$m_X^2 = (E_\gamma + m_p - E_n)^2 - (\vec{k}_\gamma - \vec{p}_n)^2, \qquad (12)$$

is the missing mass in the $\gamma p \rightarrow \pi^+ n$ reaction, assuming that the proton is at rest.

At photon energies above about 0.6 GeV, the pion singularity appears clearly ($m_X^2/m_\pi^2 \simeq 1$) in both the experimental distributions and the model results. At high energy, the magnitudes of the two peaks are comparable but the shift of the theoretical one with respect to the experimental one reflects the approximate treatment of Fermi motion effects in the model. At lower energy, the theoretical peak is smaller than in the experiment. The inclusion of higher-lying resonances in the sequential scattering amplitude in the model will enhance the peak near $m_X^2/m_\pi^2 \simeq 1$, but will probably not fill the gap around $m_X^2/m_\pi^2 \simeq -15$ for $E_\gamma = 400$ MeV.

These findings indicate a deviation from the sequential rescattering three-body mechanisms, which may be a hint in the search for more genuine three-body processes.

4. Quasi-two-body breakup

The third region of the Dalitz plot examined corresponds to the quasi-two-body breakup, where a proton and an unbound deuteron (a pn pair) are emitted back-to-back in the center-of-mass frame. For this kind of event, one of the two protons (p_1) is emitted with 2/3 of the total available energy, and the pn pair travels in the opposite direction, with 1/3 of the total energy, and with $T_{p2} = T_n = \frac{1}{6}T$. This kinematics cor-
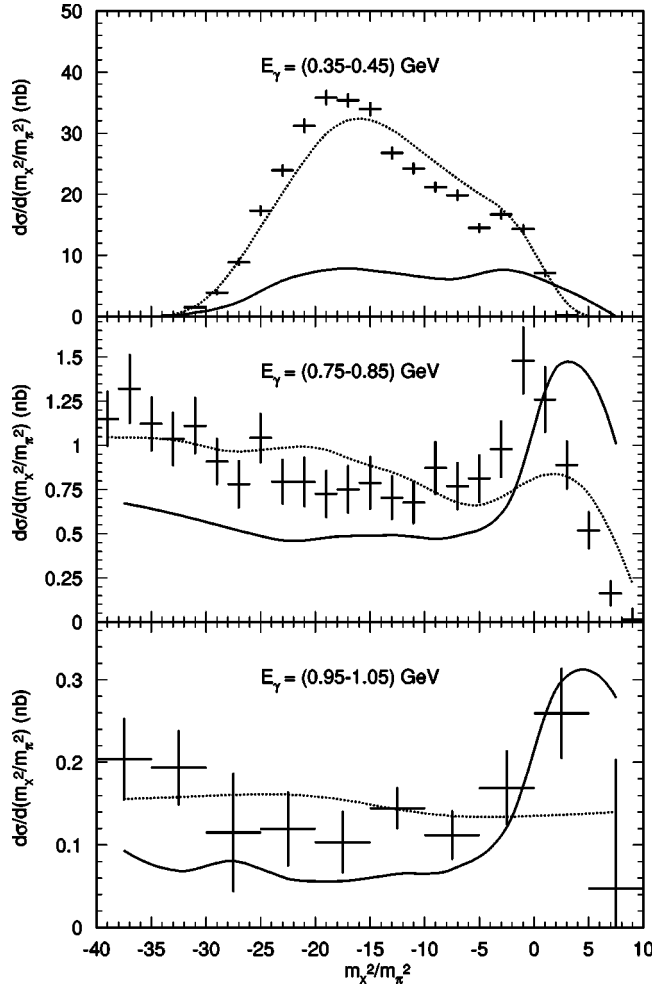
FIG. 21. Distributions of m_X^2/m_π^2 [see Eq. (12)] for the star configuration exemplified by three 0.1-GeV-wide photon-energy bins. The dotted lines represent the phase-space predictions, multiplied by the constants used to normalize the full-Dalitz cross sections, while the solid curves are the full-model results.

responds to the events in the two populated areas shown in Fig. 22. These areas have been selected by requiring that the angle between the high-energy proton and each of the other two nucleons be close to 180°, and that the difference between the energies of the two low-energy nucleons be small. Using the formalism defined above,

$$|\theta_{p1p2} - 180°| < 20°,$$

$$|\theta_{p1n} - 180°| < 20°, \qquad (13)$$

and

$$\frac{|T_{p2} - T_n|}{T} < 0.15$$

for the events on the right side of the Dalitz plot (where the proton labeled $p1$ has higher energy), and
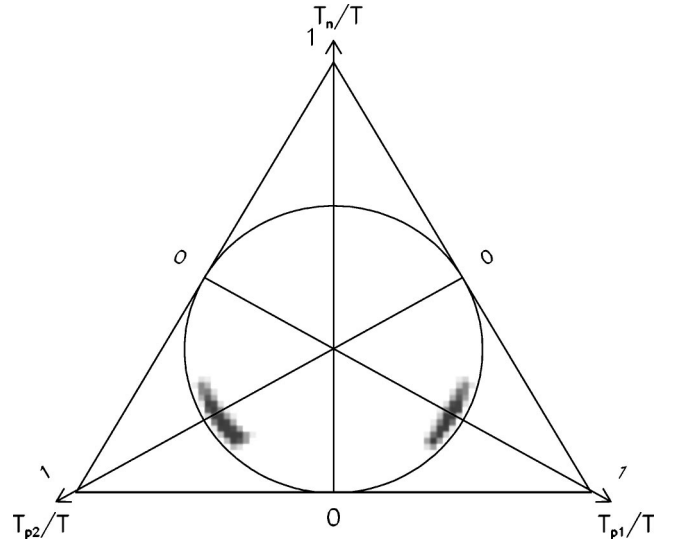
$$|\theta_{p1p2} - 180°| < 20°,$$

FIG. 22. Dalitz plot for our CLAS ppn events selected as quasi-two-body breakup.

$$|\theta_{p2n} - 180°| < 20°, \qquad (14)$$

and

$$\frac{|T_{p1} - T_n|}{T} < 0.15$$

for the events on the left side of the Dalitz plot. Since protons "1" and "2" are indistinguishable, the two regions of the Dalitz plot are equivalent.
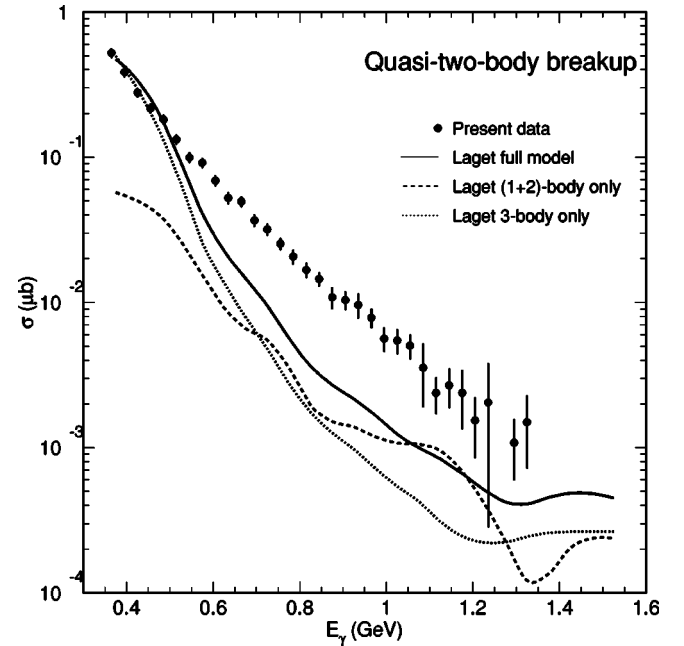

FIG. 23. Cross section integrated over the CLAS for the quasi-two-body breakup plotted as a function of photon energy. The data are compared with the predictions of the full model (solid curve), the $(1+2)$-body calculation (dashed curve), and the three-body-only calculation (dotted curve). The full-model calculation agrees quantitatively with our experimental results only up to about 0.55 GeV.
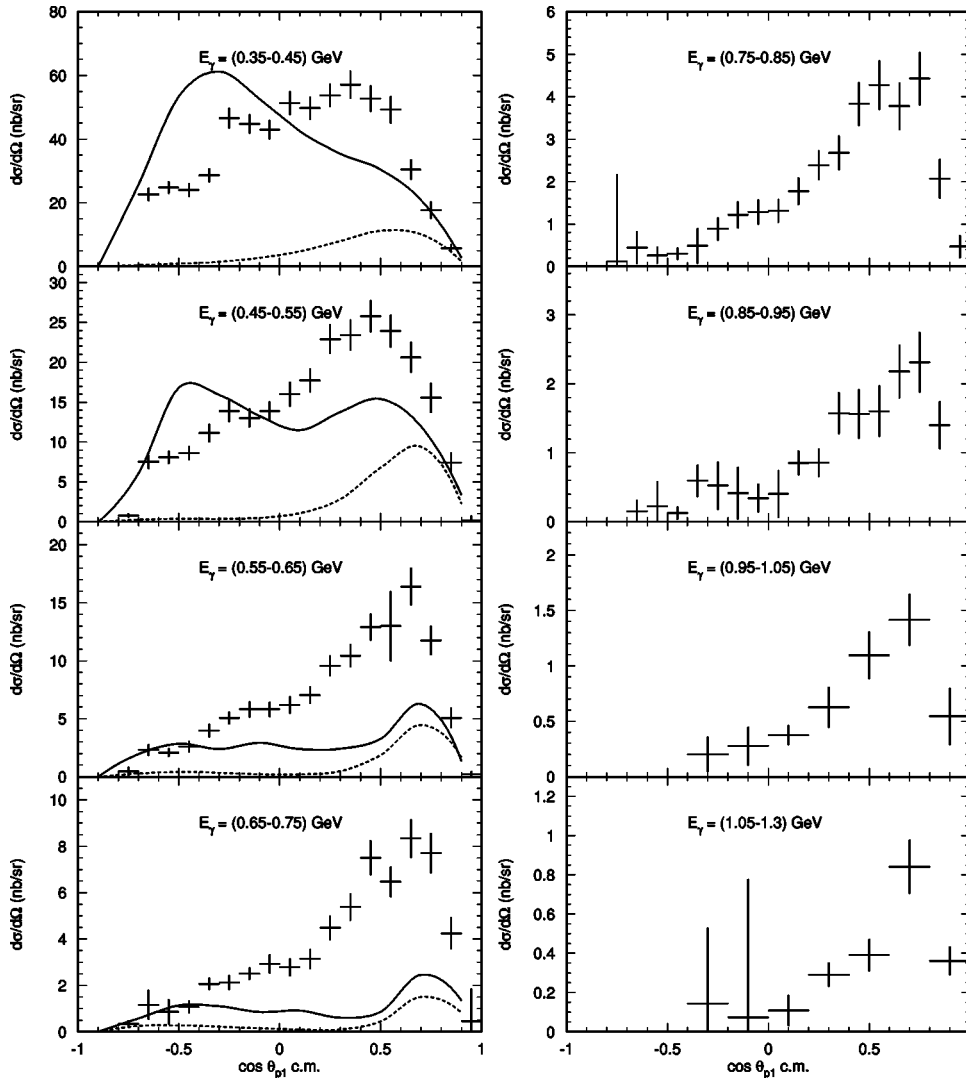
FIG. 24. Differential sections integrated over the CLAS for the quasi-two-body breakup with respect to cos θ of the high-energy proton in the center-of-mass frame for photon energies between 0.35 and 1.30 GeV. Our data, for $0.35 < E_\gamma < 0.75$ GeV, are compared with the results of the full model (solid curves) and of the $(1+2)$-body-only model (dashed curves).

In Fig. 23, the CLAS-integrated cross section for this process is plotted as a function of photon energy. It decreases exponentially with a much steeper slope than for the other kinematics ($b \simeq 7.3$ GeV^{-1}). The full-model result is in good agreement with the experimental cross section only for the low part of the photon energy range, and seriously underestimates it above about $E_\gamma = 0.55$ GeV. The $(1+2)$-body calculation gives a cross section that is smaller than the data by a factor of 5 or more for all photon energies. However, this kinematic region is expected to be strongly influenced by final-state interactions (FSI) [14]. Only S-wave NN scattering has been included in the model calculation. Furthermore, a factorization approximation has been made to estimate the ninefold integral in Fig. 8, graph (i). A full treatment, in the terms of Ref. [33], might help to reduce the discrepancy between the data and the model predictions.

It also turns out that the logarithmic singularity in the two-step sequential scattering [Figs. 8(g) and 8(h)] moves in the Dalitz plot as the photon energy varies. At lower photon energies, around $E_\gamma = 500$ MeV, it coincides with the part of the Dalitz plot where the quasi-two-body events are located and where the amplitude includes a significant contribution from FSI as well. As the photon energy increases, the singu-

larity moves toward the top of the Dalitz plot, and the contribution of sequential scattering to the quasi-two-body cross section becomes negligible. Here, the difference between the experimental cross section and the full-model result is a strong hint of a possible contribution of other three-body mechanisms that do not reduce to sequential scattering.

In Fig. 24, the differential cross section is plotted as a function of the cosine of the polar angle of the higher-energy proton in the three-body center-of-mass frame. Data from eight photon-energy bins between 0.35 and 1.30 GeV are shown. The experimental cross section shows a forward peak whose relative strength grows with increasing photon energy. This feature is also seen in the $(1+2)$-body model and in the full calculation for $E_\gamma > 0.55$ GeV. The predicted strength of the forward peak is, however, much too small to match the data. For lower energies, the full calculation predicts a cross-section enhancement at backward angles that is not seen in the data.

B. The *ppn* "three-body" cross section

Previous experiments measuring the $\gamma^3\text{He} \rightarrow ppn$ channel in an extended part of the phase space have been performed

TABLE II. Selection cuts applied to the TAGX, DAPHNE, and CLAS $\gamma\,{}^3\mathrm{He}\to ppn$ experiments in order to extract the "three-body" total cross section.

TAGX	DAPHNE	CLAS
$15° \leqslant \theta_{p1,p2} \leqslant 165°$	$22° \leqslant \theta_{p1,p2} \leqslant 158°$	$15° \leqslant \theta_{1p1,p2} \leqslant 125°$
$0° \leqslant \phi_{p1,p2} \leqslant 40°$	$0° \leqslant \phi_{p1,p2} \leqslant 360°$	CLAS ϕ fiducial cuts
$p_{p1,p2} \geqslant 300$ MeV/c	$p_{p1,p2} \geqslant 300$ MeV/c	$p_{p1,p2} \geqslant 300$ MeV/c
"Nonspectator" neutron	$p_n \geqslant 150$ MeV/c	$p_n \geqslant 150$ MeV/c

with the DAPHNE [18] and TAGX [16] detectors. Except for differences in the ϕ coverage, the CLAS event-selection cuts are very similar to the other two experiments, as seen in Table II; however, differences in the selection criteria of the three-body events exist between the TAGX experiment on the one hand and the DAPHNE and CLAS experiments on the other.

The ppn "three-body" cross section is defined as

$$\sigma_{3body}(E_\gamma) = \frac{N_{3body}(E_\gamma)}{N_\gamma(E_\gamma)Acc(E_\gamma)\dfrac{\rho z N_A}{A}}, \qquad (15)$$

where N_{3body} is the number of events extracted by applying the selection cuts given in Table II and Acc is the acceptance of the CLAS detector for the ppn events calculated with the phase-space Monte Carlo simulation. The low-momentum neutrons ($p_n \leqslant 150$ MeV/c) have been excluded in order to select only those events for which all three particles participate in the reaction, thus diminishing the importance of two-body processes [16,18]. In this kinematics, the phase-space result describes the process reasonably well.

Figure 25 shows σ_{3body} as a function of the photon energy E_γ. The full circles represent our CLAS data, the empty triangles the data of the TAGX Collaboration [16], and the empty squares the results obtained in the experiment carried out at MAMI with the DAPHNE detector [18]. The error bars on the CLAS data are statistical only. The systematic uncertainties delineated in the previous section are shown by the vertical lines in the upper part of the figure.

In the overlap region of the three experiments from 0.35 to 0.80 GeV, the CLAS data are in good agreement with the DAPHNE results, but differ from the TAGX cross sections by about 15%, most likely due to the above-mentioned difference in the three-body event selection. Above 0.80 GeV, no previous data are available.

The phase-space extrapolation to the unmeasured regions has been done only for comparison with the previous experiments, which adopted the same procedure to extract σ_{3body}.

VI. SUMMARY AND CONCLUSIONS

The three-body photodisintegration of ${}^3\mathrm{He}$ has been measured with the tagged-photon beam and the CEBAF Large Acceptance Spectrometer in Hall B at the Thomas Jefferson National Accelerator Facility in the photon-energy range between 0.35 and 1.55 GeV. This measurement constitutes a wide-ranging survey of two- and three-body processes in the

$\gamma\,{}^3\mathrm{He}\to ppn$ reaction channel, as a consequence of the high statistics and large kinematic coverage obtained with the CLAS.

Total and partially integrated differential cross sections for the full ppn data set and for selected kinematics were extracted and are compared with phase-space distributions and with the predictions of the diagrammatic model of Laget. This model reproduces some of the main trends of the experimental energy distributions, and for these cases can be taken as a qualitative guide to understanding the reaction mechanisms.

From the analysis of the neutron-momentum distribution for the full Dalitz plot, the kinematic region corresponding to the photodisintegration of a pp pair in the presence of a spectator neutron has been identified. Here, the effects of two-body absorption mechanisms dominate and the model results are very close to experiment at low energy, up to $E_\gamma=600$ MeV. At higher energies, the discrepancy, which increases with energy, might be a hint that we are approach-

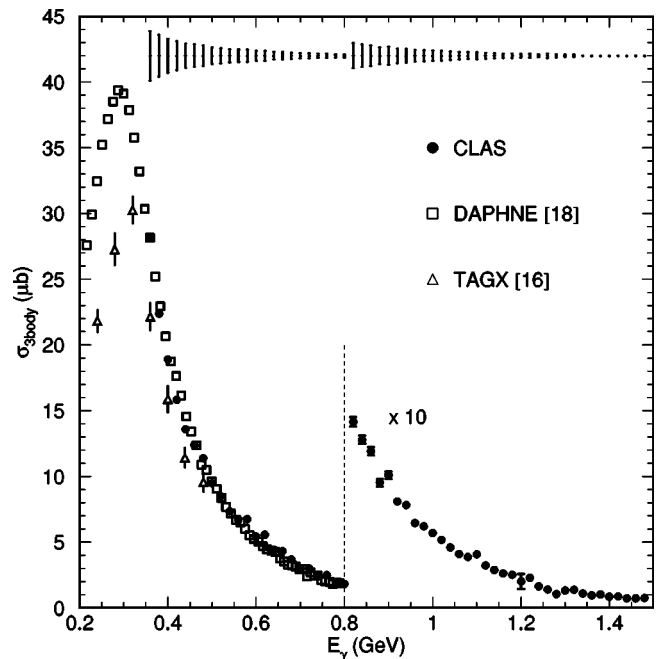FIG. 25. Total "three-body" cross section as defined by Eq. (15) for the $\gamma\,{}^3\mathrm{He}\to ppn$ reaction plotted as a function of photon energy. The CLAS data (full circles) are compared with the results from DAPHNE [18] (empty squares) and TAGX [16] (empty triangles). The error bars on the CLAS experimental points are statistical only. The CLAS systematic uncertainties are represented by the vertical bars in the upper part of the figure.

ing the limit of models based on meson and baryon degrees of freedom.

A strong contribution of three-body sequential meson-absorption mechanisms is manifested over all the available phase space, but most especially in the *star* kinematics, the spatially symmetric configuration of the three final-state nucleons. These events are dominated by the coupling to the Δ resonance, and they strongly confirm its role in three-body forces. The deviations from the predictions of the diagrammatic model point not only toward the necessity of implementing processes which involve higher-lying baryonic resonances, but also toward possible additional three-body mechanisms beyond sequential scattering.

The 4π-integrated "three-body" cross section is in excellent agreement with previous experimental results from DAPHNE up to 800 MeV. For the first time we now have provided access to a higher energy range, up to 1.5 GeV.

This work breaks new ground in the experimental study of the three-body photodisintegration of ^{3}He. However, before making contact with the elusive three-body forces, it calls for a more complete treatment of three-body mechanisms which go beyond the dominant sequential meson exchange and Δ formation in the intermediate energy range, and which take into account possible coupling with partonic degrees of freedom in the highest energy range.

[1] *Proceedings of the Three-Body Force in the Three-Nucleon System*, edited by B. L. Berman and B. F. Gibson (Springer, Berlin, 1986).

[2] *Proceedings of the Seventeenth International IUPAP Conference on Few-Body Problems in Physics (Few-Body 17)*, edited by W. Glöckle and W. Tornow (Elsevier, Amsterdam, 2004).

[3] J. M. Laget, J. Phys. G **14**, 1445 (1988).

[4] J. M. Laget, in *New Vistas in Electronuclear Physics*, edited by E. Tomusiak, H. Caplan, and E. Dressler (Plenum, New York, 1986), p. 361.

[5] J. M. Laget, in *Modern Topics in Electron Scattering*, edited by B. Frois and I. Sick (World Scientific, Singapore, 1991), p. 290.

[6] W. Glöckle *et al.*, Phys. Rep. **274**, 107 (1996).

[7] E. Epelbaum *et al.*, Phys. Rev. C **66**, 064001 (2002).

[8] J. M. Laget, Phys. Rep. **69**, 1 (1981).

[9] J. M. Laget, Nucl. Phys. **A446**, 489c (1985).

[10] J. M. Laget, Phys. Rev. C **35**, 832 (1987).

[11] J. M. Laget, Nucl. Phys. **A497**, 391c (1989).

[12] B. L. Berman, L. J. Koester, Jr., and J. H. Smith, Phys. Rev. **133**, 117 (1964).

[13] G. Audit *et al.*, Phys. Rev. C **44**, R575 (1991).

[14] A. J. Sarty *et al.*, Phys. Rev. C **47**, 459 (1992).

[15] G. Audit *et al.*, Phys. Lett. B **312**, 57 (1993).

[16] T. Emura *et al.*, Phys. Rev. Lett. **73**, 404 (1994).

[17] N. R. Kolb *et al.*, Phys. Rev. C **54**, 2175 (1996).

[18] G. Audit *et al.*, Nucl. Phys. **A614**, 461 (1997).

[19] S. Niccolai, Ph.D. dissertation, The George Washington University (2003).

[20] B. Mecking *et al.*, Nucl. Instrum. Methods Phys. Res. A **503**, 513 (2003).

[21] D. Sober *et al.*, Nucl. Instrum. Methods Phys. Res. A **440**, 263 (2000).

[22] C. Hajduk and P. U. Sauer, Nucl. Phys. **A369**, 321 (1981).

[23] M. Lacombe *et al.*, Phys. Rev. C **21**, 861 (1980).

[24] J. M. Laget, Phys. Rev. C **38**, 2993 (1988).

[25] J. M. Laget, Phys. Lett. **151B**, 325 (1985).

[26] J. M. Laget, Phys. Lett. B **199**, 493 (1987).

[27] J. K. Aniol *et al.*, Phys. Rev. C **33**, 1714 (1986).

[28] S. J. Brodsky *et al.*, Phys. Lett. B **578**, 69 (2004).

[29] E. C. Schulte *et al.*, Phys. Rev. C **66**, 042201 (2002).

[30] V. Y. Grishina *et al.*, Eur. Phys. J. A **A10**, 355 (2001).

[31] J. Blomqvist and J. M. Laget, Nucl. Phys. **A280**, 405 (1977).

[32] M. Guidal, J. M. Laget, and M. Vanderhaeghen, Nucl. Phys. **A627**, 645 (1997).

[33] J. M. Laget, Few-Body Syst., Suppl. **15**, 171 (2003).